Supporting Information

Type-II Heterojunction Photocathode for CO_2 reduction and Light-Assisted Metal-CO_2 Batteries

Yanbin Zhu, Yan Wei, Peize Li, Shujie Liu, Jiandong Zhang, Liyuan Tian, Pengkun Gao, Yali Zhang, Jie Li, Deyu Wang, Yan Shen [*], and Mingkui Wang [*]

Y. Zhu, Y. Wei, P. Li, S. Liu, J. Zhang, L. Tian, Prof. Y. Shen, Prof. M. Wang

Wuhan National Laboratory for Optoelectronics, Huazhong University of Science and Technology, Wuhan 430074, P.R. China

Email: ciac_sheny@mail.hust.edu.cn, mingkui.wang@mail.hust.edu.cn

P. Gao, Y. Zhang, J. Li

PYTES (ShanDong) Energy Technology Co. Ltd., Building 1, High-tech industrial park, No.36 East Dongfeng Road, Weishan County, Jining, Shandong, 277600 P. R. China

Prof. D. Wang

Key Laboratory of Optoelectronic Chemical Materials and Devices (Ministry of Education), School of Chemical and Environmental Engineering, Jianghan University, Wuhan 430056, China
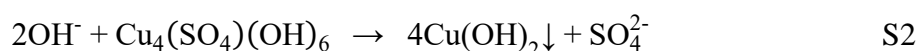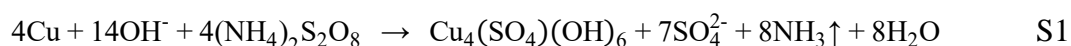
Experimental section

1. Chemicals and materials

All raw materials, reagents and solvents used in the synthesis and performance evaluation of the target samples in this experiment were purchased directly from the following companies and were not further purified. Sodium hydroxide (NaOH), Ammonium persulphate $((NH_4)_2S_2O_8$, AR), Ferric nitrate nonahydrate $(Fe(NO_3)_3·9H_2O$, AR), Acetonitrile $(CH_3CN$, AR) were purchased from Sinopharm Chemical Reagent Co., Ltd. Tetrabutylammonium hexafluorophosphate $(C_{16}H_{36}N·PF_6$, 98%) was purchased from Shanghai Aladdin Biochemical Technology Co., Ltd. The deionized water used in the whole experimental process was taken from Milli-Q Integral 3 instrument (18.3 MΩ·cm^{-1}).

2. Material preparation

2.1 Fe_2O_3/Cu_2O nanowires

Herein, we adopted a "wet chemical method" to prepare the required catalysts. First, copper mesh (300 mesh) was ultrasonically cleaned with 0.5 M H_2SO_4 for 2~5 min to remove surface impurities. The above cleaned copper mesh (1×4 cm^{-2}) was placed vertically in a 100 mL mixed solution containing 10 g sodium hydroxide and 2.7 g ammonium persulphate. The copper mesh is continuously oxidized and dissolved by ammonium persulphate in alkaline solutions. The dissolved Cu^{2+} reacted with the OH$^-$ and $S_2O_8^{2-}$ in the above-mentioned mixed solution to form a blue film as shown in Equation S1. Then, the color of the blue film gradually deepened and $Cu(OH)_2$ nanowires formed on the copper mesh (Equation S2), coded as $Cu(OH)_2$. The reaction time for this process has been optimized to 15 min.

$$4Cu + 14OH^- + 4(NH_4)_2S_2O_8 \rightarrow Cu_4(SO_4)(OH)_6 + 7SO_4^{2-} + 8NH_3\uparrow + 8H_2O \qquad S1$$

$$2OH^- + Cu_4(SO_4)(OH)_6 \rightarrow 4Cu(OH)_2\downarrow + SO_4^{2-} \qquad S2$$

Immediately afterwards, the obtained $Cu(OH)_2$ nanowires were immersed in a 0.1 mM $Fe(NO_3)_3·9H_2O$ solution. Because the solubility of $Fe(OH)_3$ is relatively low ($K_{sp} = 2.6 \times 10^{-39}$) and the hydrolysis process around $Cu(OH)_2$ nanowires is enhanced. During immersion process, the hydrolysis of Fe^{3+} occurred preferentially around $Cu(OH)_2$ nanowires to form $Fe(OH)_3$ colloid, as the following equation S3. Finally, the $Fe(OH)_3$ formed by hydrolysis was wrapped around the surface of $Cu(OH)_2$ nanowires, coded as $Fe(OH)_3/Cu(OH)_2$.

$$Fe^{3+} + 3H_2O \rightarrow Fe(OH)_3 + 3H^+ \qquad S3$$

The as-prepared $Fe(OH)_3/Cu(OH)_2$ nanowires were transferred to a tube furnace and heated to 450 °C at a rate of 5 °C min^{-1} for 5 h under a high purity nitrogen gas flow. The required catalysts of Fe_2O_3/Cu_2O nanowires were obtained by subsequent cooling to room temperature.

2.2 Cu$_2$O nanowires

The synthesis process of Cu$_2$O nanowires was the same as that of Fe$_2$O$_3$/Cu$_2$O nanowires, except of immersion the pre-prepared Cu(OH)$_2$ nanowires into the Fe(NO$_3$)$_3\cdot$9H$_2$O solution. The formation of Cu$_2$O rather than CuO after heat treatment of Cu(OH)$_2$ nanowires in this study can be attributed to the negligible oxygen concentration and the insufficient partial pressure of oxygen in N$_2$ atmosphere and high temperature conditions, which causes Cu(OH)$_2$ to lose water molecules along with oxygen.[1]

3. Materials characterization

The crystal structure of the copper mesh grown with different complexes was recorded using a powder X-ray diffractometer (PXRD, X'Pert3 Powder, purchased from PANalytical B.V.) equipped with Cu Kα radiation (λ = 1.54060 Å) ranging from 5 to 90° at room temperature. The microscopic morphology, size and array characteristics of the above synthesized samples was measured using a field emission scanning electron microscope (FSEM, FEI Netherlands Sirion 200). The structural features of the Fe$_2$O$_3$/Cu$_2$O nanowires were performed using a field emission transmission electron microscope (FTEM, FEI Netherlands Tecnai G2 F30) equipped with energy dispersive X-ray spectroscopy (EDX, Oxford XPLORE). X-ray photoelectron spectrometer (XPS, Thermo Scientific Escalab 250Xi) was used to analyze the surface chemical state of the above synthesized samples. The absorbance properties of the Cu$_2$O/Cu and Fe$_2$O$_3$/Cu$_2$O/Cu samples were tested by a UV–vis spectrophotometer (UV-3600, Shimadzu, Japan) ranging from 350 to 800 nm. Photoluminescence spectroscopy and Raman spectra of the above samples were obtained by Raman spectrometer at a 532 nm excitation wavelength of a 30 mW HE-Cd laser. The SECM experiments were carried out on CHI 920C electrochemical workstation (CH Instruments, Shanghai, China). The detailed fabrication steps and measurement procedures have been reported in our previous literature.[2,3]

4. Density functional theory (DFT) calculations

We have employed the Vienna Ab Initio Package (VASP)[4,5] to perform the density functional theory (DFT) calculations within the generalized gradient approximation (GGA) using the PBE[6] formulation. We have chosen the projected augmented wave (PAW) potentials[7,8] to describe the ionic cores and take valence electrons into account using a plane wave basis set with a kinetic energy cutoff of 450 eV. Partial occupancies of the Kohn-Sham orbitals were allowed using the Gaussian smearing method and a width of 0.05 eV. The electronic energy was considered self-consistent when the energy change was smaller than 10^{-4} eV. A geometry optimization was considered convergent when the force change was smaller than 0.05 eV/Å.

According to the XRD data for Cu_2O with cubic phase, the main exposed surface is Cu_2O (111). The (200) surface of Fe_2O_3 is used to construct a heterojunction composite structure with a lattice mismatch of less than 6%, which basically satisfies the heterojunction requirements with reasonable computational power.

5. CO_2 reduction and conversion performance evaluation

5.1 Photoelectric reduction CO_2 measurement

The performance evaluation of photoelectric reduction CO_2 was realized in the photoelectrochemical performance test platform built by our group. The measurement equipment consists of a full spectrum 300 W Xenon lamp (Newport, 69911, USA), chopper, light filter (AM 1.5G), electrochemical workstation and optoelectrolytic cell. The above-mentioned photoelectrolytic cell is a customized double-chamber H-type electrolytic cell containing working electrode, reference electrode (saturated calomel electrode), counter electrode (platinum wire) and proton exchange membrane (Nafion 117). In the experiments, 0.1 M acetonitrile solution of tetrabutylammonium hexafluorophosphate ($C_{16}H_{36}N \cdot PF_6$) containing a small amount of water (35 ml acetonitrile + 200 µl water for cathode cell) was used as the electrolyte. The role of water in the electrolyte is to provide protons, and numerous literatures have reported this role.[9-11] High-purity CO_2 (99.999%) was injected into the electrolyte for 10 min before linear sweep voltammetry and chronoamperometry i-t tests were performed. A gas chromatograph (Agilent GC-2020) equipped with a Pora PLOT Q column and a molecular sieve column was performed for qualitative analysis of gaseous products. The GC configuration includes a fame ionization detector (FID) with methanizer and thermal conductivity detector (TCD) with N_2 carrier gas. The Faraday efficiency of the gas-phase reduction products is calculated by the following equation:

$$FE\% = \frac{\alpha n F}{Q} \qquad\qquad S4$$

Where Q is the electric quantity consumed by the CO_2 reduction reaction during the set reaction time (C), F is the faraday constant (96485 $C \cdot mol^{-1}$), α is the number of transferred electrons required to generate the target product, n is the number of moles of the corresponding yield.

All the photoelectrocatalytic CO_2 reduction experiments were performed on the CHI 660D electrochemical workstation. Linear sweep voltammetry (LSV) curves with a scan rate of 5 $mV \cdot s^{-1}$ were used to choose the appropriate potential range for the $Fe_2O_3/Cu_2O/Cu$ photocathode. The above LSV and photoelectrocatalytic CO_2 reduction tests were carried out without *iR* compensation and under ambient conditions. As the Ag/Ag^+ electrode is not a standard reference for a nonaqueous system, the recorded potentials vs Ag/Ag^+ were converted to the ones vs Fc/Fc^+.[2]

4

5.2 Metal-CO$_2$ batteries assembly and performance evaluation

The copper mesh grown with Fe$_2$O$_3$/Cu$_2$O nanowires was cut to an electrode piece with a diameter of 12 mm and used directly as the positive electrode. No additional conductive agents, binders or collectors were required. The positive electrode piece needs to be transferred to a vacuum oven at 120°C for 12 h before being assembled. The pre-dried glass fiber separator (Whatman, GF/D) with a diameter of 19 mm was employed as the separator, lithium foil or sodium foil with a diameter of 16 mm was employed as anode. 1.0 M LiTFSI in TEGDME, 1.0 M NaPF$_6$ in mixed solvents of ethylene carbonate and dimethyl carbonate (volume ratio of 1:1, with 5% fluoroethylene carbonate) were used as electrolytes for Li-CO$_2$ and Na-CO$_2$ batteries, respectively. Stainless steel gasket and shrapnel with a diameter of 16 mm were introduced for fixing purposes. Subsequently, the above parts were assembled into the CR2032 cells with several holes on the positive side in a high-purity argon atmosphere glove box (H$_2$O < 0.1 ppm, O$_2$ < 1.0 ppm). The as-assembled batteries were placed to stand in a home-made test chamber filled with pure carbon dioxide for 8 hours before being performance evaluation. Then its discharge/charge performances were evaluated with or without illumination on the LAND CT2001A battery test system under simulated AM 1.5 G solar illumination (Xe lamp). The electrochemical impedance spectroscopy (EIS) curves of Li/Na-CO$_2$ batteries were measured though the CHI 660D electrochemical workstation in the frequency range of 10 mHz to 100 kHz.

The assembly procedure of the flexible quasi-solid-state Li-CO$_2$ pouch battery is similar to that of the above-mentioned CR2032 cells. In short, the copper mesh grown with Fe$_2$O$_3$/Cu$_2$O nanowires, lithium foil with a thick of 0.025 mm, the polypropylene separator coated with LATP electrolyte on both sides, and the aluminum-plastic film with several holes on positive side were used as positive electrode, negative electrode, electrolytes and encapsulation layers for Li-CO$_2$ pouch battery, respectively. In addition, a small amount of 1.0 M LiTFSI in TEGDME was added to the assembled Li-CO$_2$ pouch battery and its performance evolution was performed after a period of standing. The adding amount of electrolyte was 5~8% of the liquid injection amount of a standard liquid pouch battery.
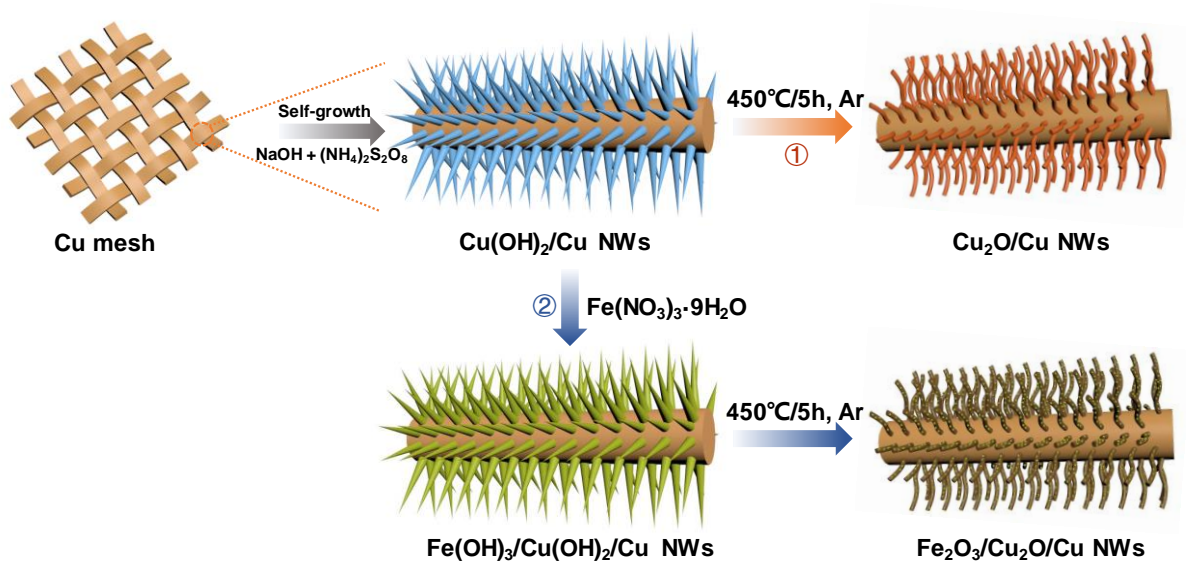
Figure S1. Schematic diagram of the synthesis process of Cu_2O and Fe_2O_3/Cu_2O nanowires (NWs).

Figure S1 schematically illustrates the synthesis processes of Fe_2O_3/Cu_2O nanowires on Cu mesh. Cu mesh (300 mesh) was selected as the substrate due to its flexibility and superior conductivity. Its microporous structure enables a through-transfer of reactants. In addition, Cu mesh can be used as a source of copper for in-situ growth of $Cu(OH)_2$ nanowires in an alkaline environment. $Cu(OH)_2$ nanowires was firstly growth onto Cu mesh surface though a room-temperature impregnation method. Afterwards, the $Fe(OH)_3$ colloids were attached onto the $Cu(OH)_2$ nanowires surface by impregnating the samples into iron nitrate aqueous solution to form $Fe(OH)_3/Cu(OH)_2$. Lastly, a high-temperature annealing treatment under argon atmosphere further produced Fe_2O_3/Cu_2O nanowires. For comparison purpose, the control sample of Cu_2O nanowires on Cu mesh substrate was also prepared without coating $Fe(OH)_3$ colloids as described above.
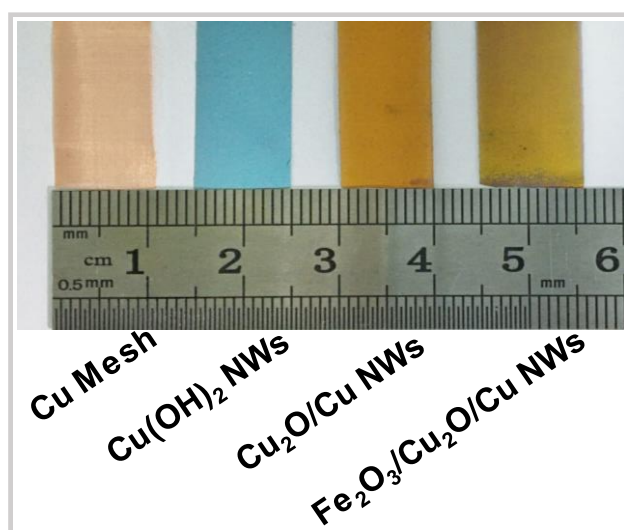
Figure S2. Optical photographs of Cu mesh, and Cu(OH)$_2$, Cu$_2$O nanowires, Fe$_2$O$_3$/Cu$_2$O nanowires on Cu meshes.
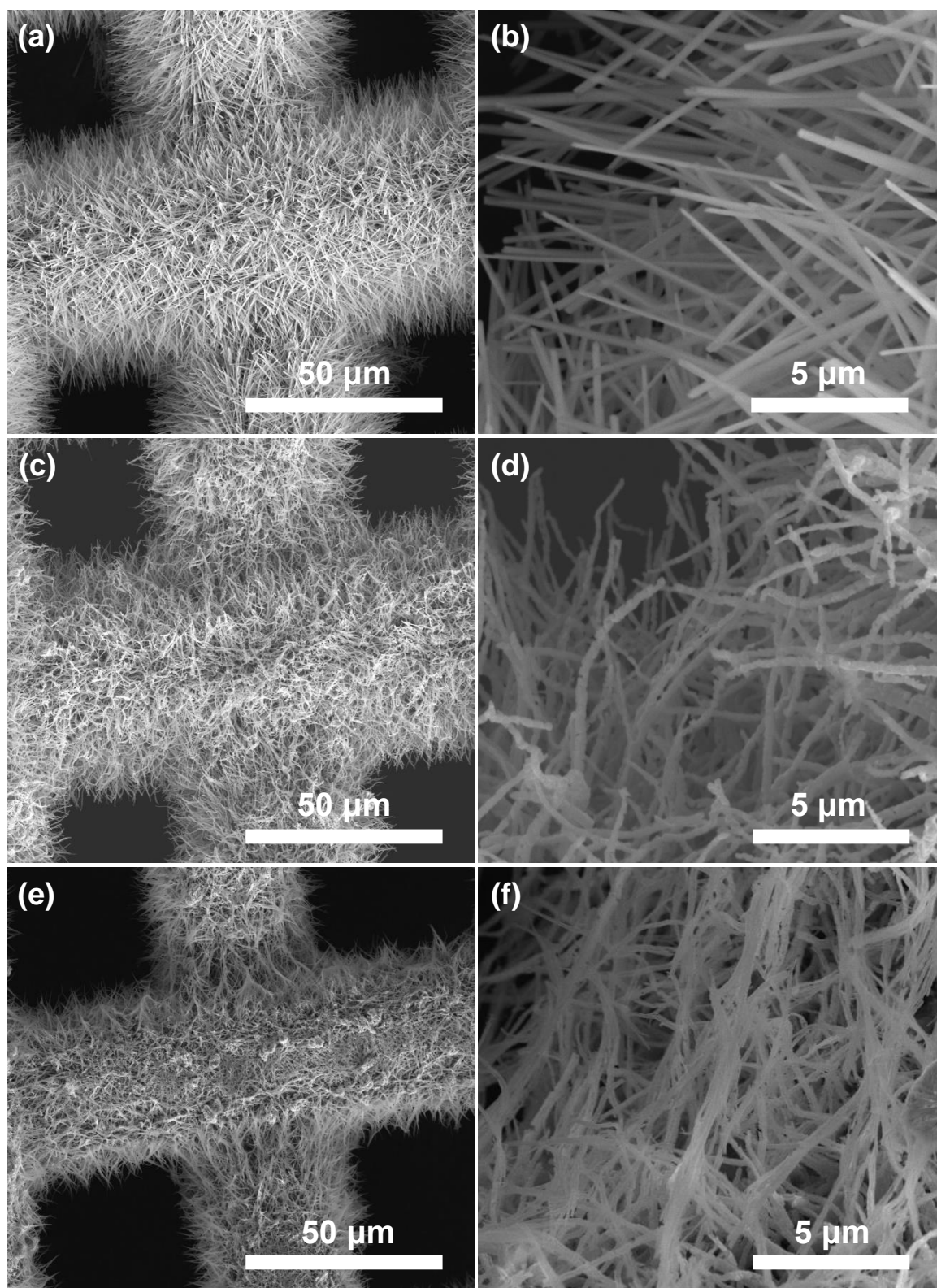
Figure S3. SEM images of (a, b) $Cu(OH)_2$ nanowires, (c, d) Cu_2O nanowires and (e, f) $Fe(OH)_3/Cu(OH)_2$ nanowires.
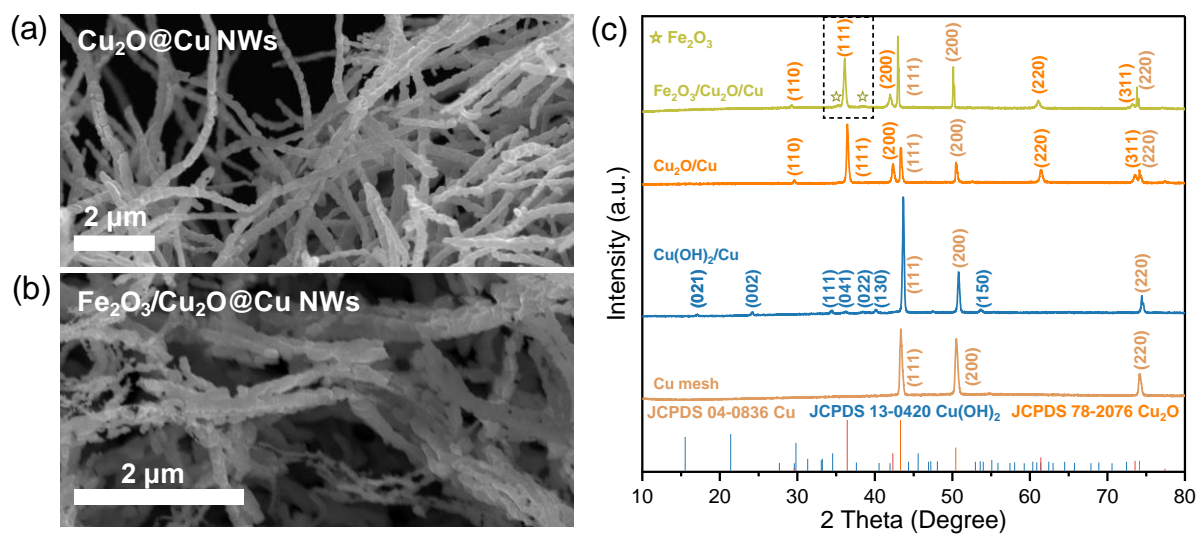
Figure S4. SEM images of (a) Cu$_2$O and (b) Fe$_2$O$_3$/Cu$_2$O nanowires. (c) XRD patterns of Cu mesh, Cu(OH)$_2$, Cu$_2$O/Cu, and Fe$_2$O$_3$/Cu$_2$O/Cu nanowires.
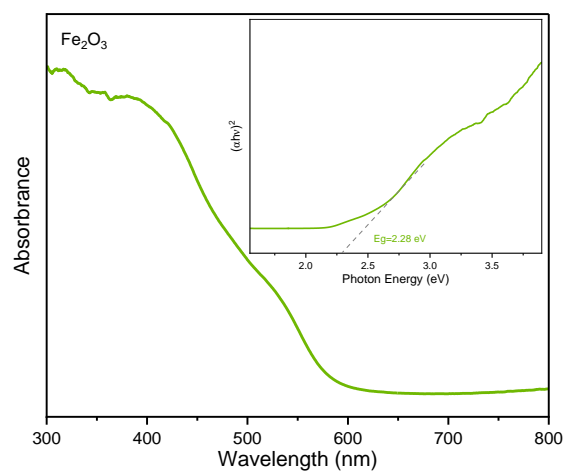
Figure S5. UV–vis diffuse reflectance spectra of the Fe_2O_3 sample, respectively. The inset is the Tauc plot.
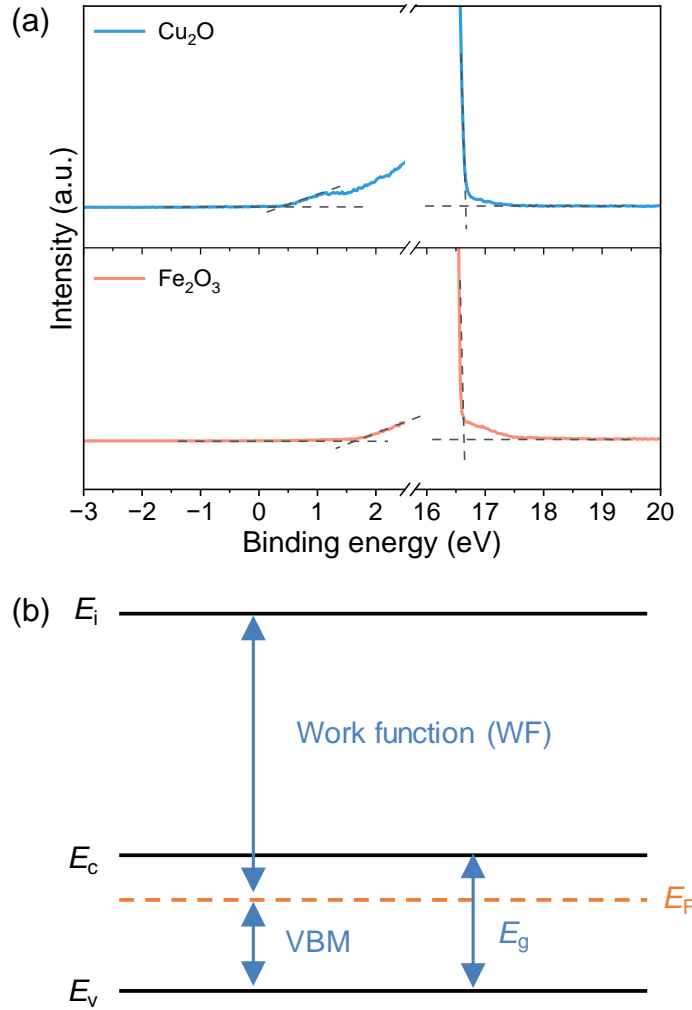
Figure S6. (a) Ultraviolet photoelectron spectra of the Cu_2O and Fe_2O_3 samples. (b) The scheme of band structure for a semiconductor material.

The relative potentials of Cu_2O and Fe_2O_3 were determined by calculating their respective energy band structures. The energy band structures of Cu_2O and Fe_2O_3 were estimated with UV-visible absorption (Figure 2d and Figure S5) and ultraviolet photoelectron spectroscopy characterizations (Figure S6a). The bandgap (E_g) of Cu_2O and Fe_2O_3 can be firstly estimated by extending the Tauc's plot (replotted from absorbance curve). The results are shown in the insets in Figure 2d, S5. Figure S6a and S6b exhibits the ultraviolet photoelectron spectroscopy and the calculated schematic of the energy band structure for the corresponding samples. The right panel displays the photoemission cutoff (E_{cutoff}) and the left panel displays the position of valence band maximum (VBM). All energies are referenced to a common vacuum level (E_i=0 eV). The work function (WF) is estimated with the equation of WF = $21.22 - (E_{cutoff} - E_i)$. The valence band ($E_V$) is extracted from formula of $E_V = E_F + $ VBM and the conduction band (E_C) can be calculated by $E_C =$ WF $+ E_V - E_g$.
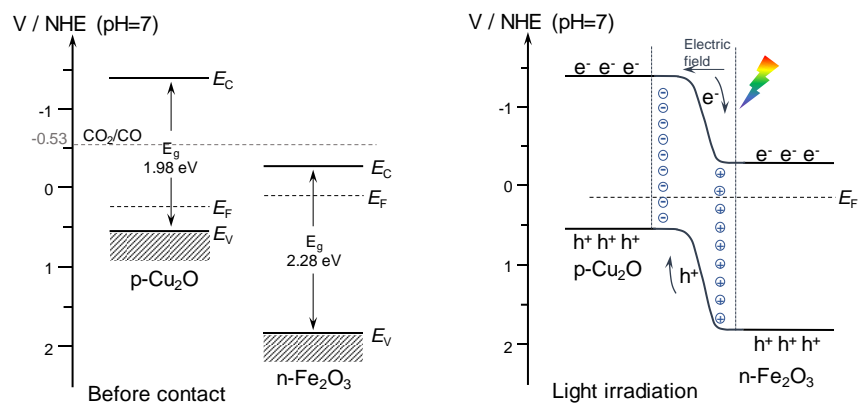
Figure S7. Band energy structure diagrams of Cu_2O and Fe_2O_3/Cu_2O nanowires.
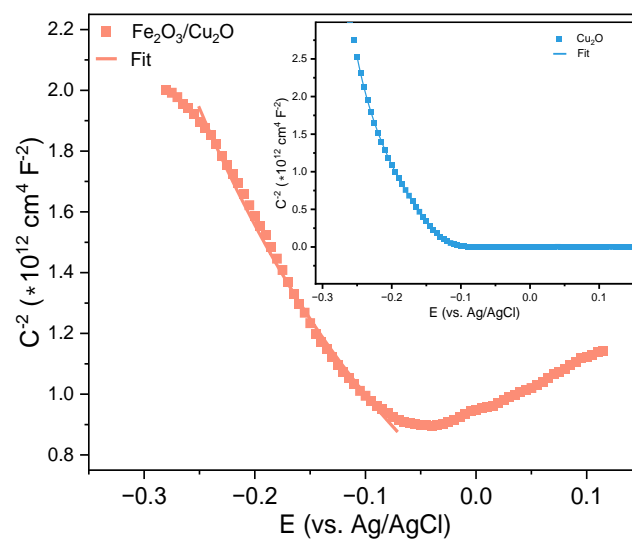
Figure S8. Mott-Schottky plots of Cu$_2$O and Fe$_2$O$_3$/Cu$_2$O nanowires.
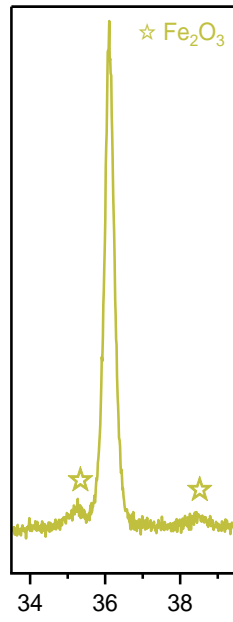
☆ Fe₂O₃

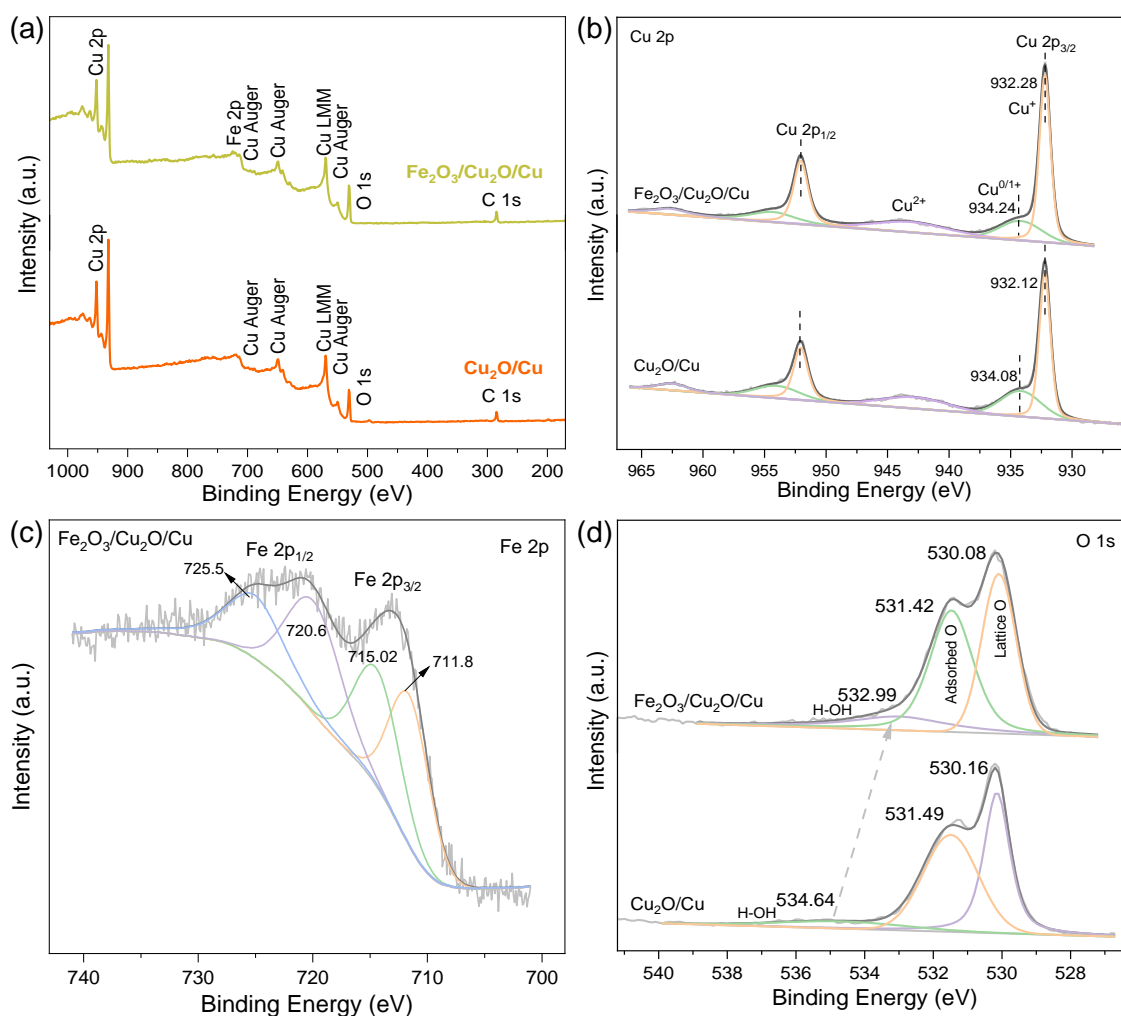**Figure S9.** Enlarged XRD image of Fe$_2$O$_3$/Cu$_2$O nanowires in the range of 33° to 40°.

Figure S10. High-resolution XPS spectra of Cu_2O and Fe_2O_3/Cu_2O nanowires. (a) XPS survey spectra. (b) Cu 2p, (c) Fe 2p and (d) O 1s XPS spectra and the corresponding fitting results.

The surface chemical state and electronic properties of the above-mentioned samples were studied using X-ray photoelectron spectroscopy (XPS). The XPS survey revealed that the Fe_2O_3/Cu_2O nanowires contained only elemental Cu, Fe, O, and C (Figure S10a). The high-resolution Cu 2p spectra presented in Figure S10b showed that the peaks located at ~932 eV and ~952 eV binding energy could be assigned to the Cu $2p_{3/2}$ and Cu $2p_{1/2}$ peaks of Cu^+, respectively.[3] The signal of peak at ~943 eV can be attributed to Cu^{2+}, which is caused by the slight oxidation of Cu_2O surface in the air. Fe 2p XPS spectra further confirm the presence of Fe^{3+} in Fe_2O_3/Cu_2O nanowires (Figure S10b).[12] The O 1s XPS signal of Fe_2O_3/Cu_2O showed a lower proportion of peak (representing the adsorbed oxygen at ~ 531 eV) and a shift towards lower binding energy of peak (representing the oxygen-containing groups in the adsorbed water at ~ 534 eV), suggesting the inhibition of surface oxidation and water absorption by Fe_2O_3 on Cu_2O and thus maintaining the valence of Cu^+ (Figure S10d).[13]
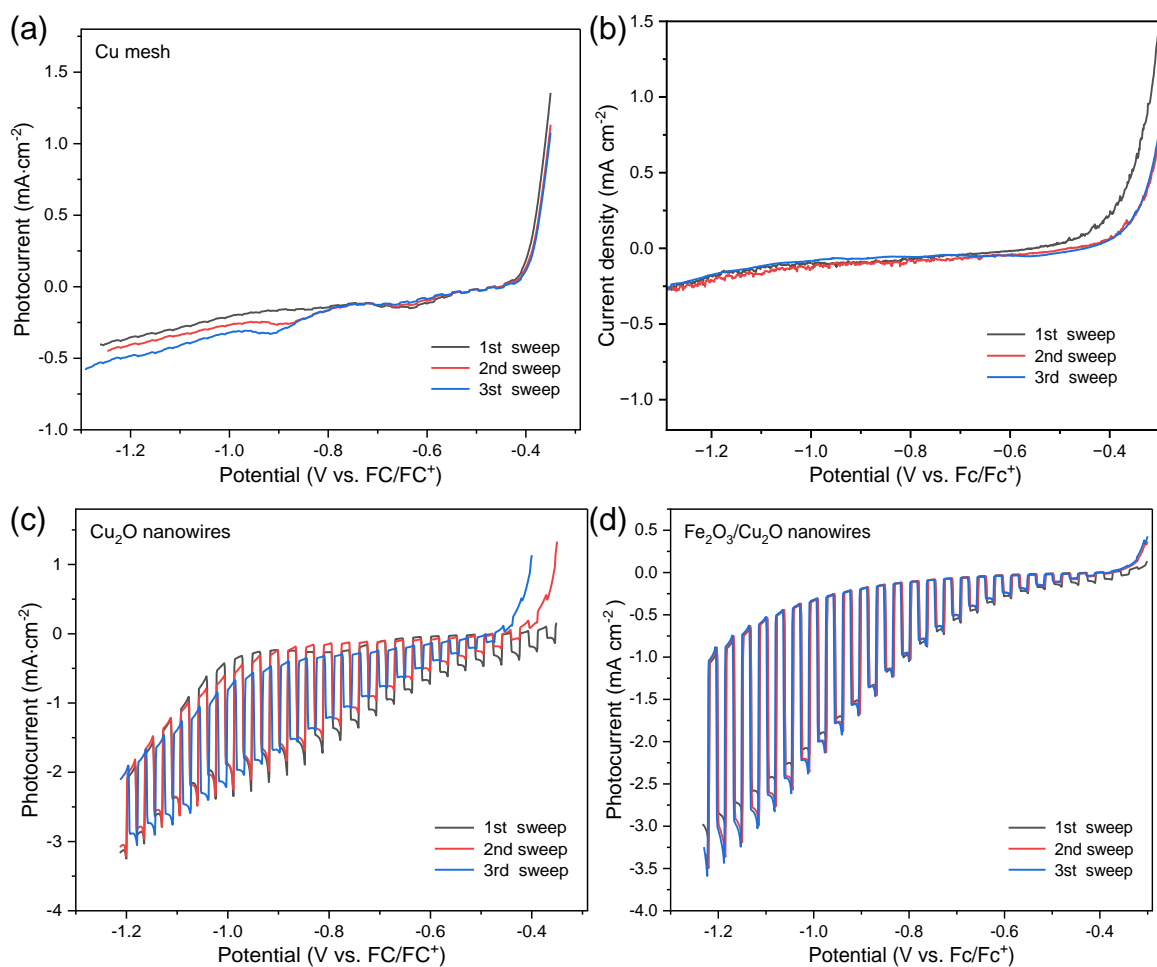
Figure S11. Linear sweep voltammetry curves with different sweeps in CO_2-saturated 1.0 M tetrabutylammonium hexafluorophosphate in acetonitrile under chopped light illumination. (a) Cu mesh, (b) Fe_2O_3 sample, (c) Cu_2O nanowires and (d) Fe_2O_3/Cu_2O nanowires photocathodes.
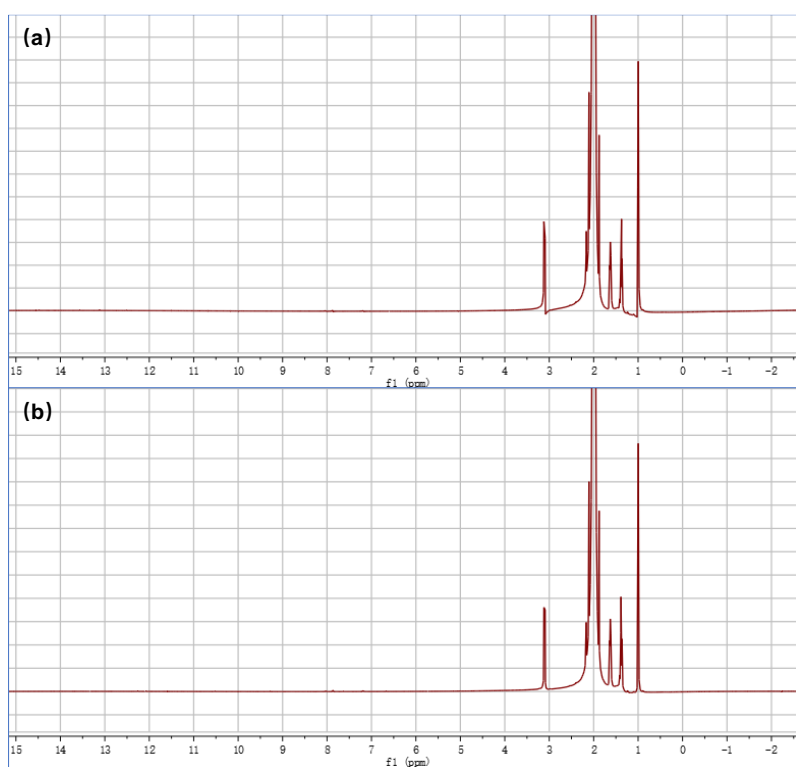
Figure S12. ^{1}H NMR spectra of (a) the fresh electrolyte, (b) the electrolyte after the PEC CO$_2$RR for Fe$_2$O$_3$/Cu$_2$O nanowire electrode at -1.0 V (vs. Fc/Fc$^+$) for 10 min. The electrolyte is CO$_2$ saturated 1.0 M tetrabutylammonium hexafluorophosphate in acetonitrile.
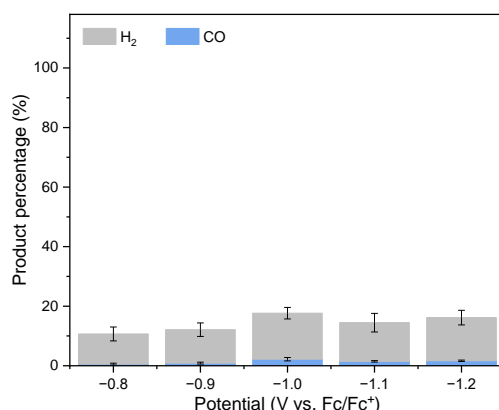
Figure S13. (c) Product percentage of Fe_2O_3 sample at a potential ranging from -0.8 V to -1.2 V (vs. Fc/Fc^+) in CO_2 saturated 1.0 M tetrabutylammonium hexafluorophosphate in acetonitrile.

To evaluate the product selectivity of Fe_2O_3/Cu_2O nanowire for CO_2RR, the reduction products were quantitatively analyzed using gas chromatography and liquid nuclear magnetic resonance (^1H NMR) spectrometer. The gas phase products were identified to be CO and H_2 (Figure 3c), while the liquid phase products were essentially not produced (Figure S13). The Fe_2O_3/Cu_2O nanowire electrode shows a high selectivity of over 89% for CO in the applied potential (-0.8 to -1.2 V vs. Fc/Fc^+) and up to 94% at -0.8 V (vs. Fc/Fc^+). Additionally, we also carried out the performance evaluation of photoelectrochemical CO_2 reduction catalyzed by Fe_2O_3 sample. According to the LSV curves provided in Figure S11b, it can be seen that the n-type Fe_2O_3 sample are essentially no photo response to photoelectrochemical CO_2 reduction. The reduction products in the range of applied reduction potentials are mainly hydrogen and a small amount of CO (Figure S13) and the percentage of products is less than 20%. We speculate that this may be due to the fact that most of the charge was consumed by the n-type Fe_2O_3 itself.
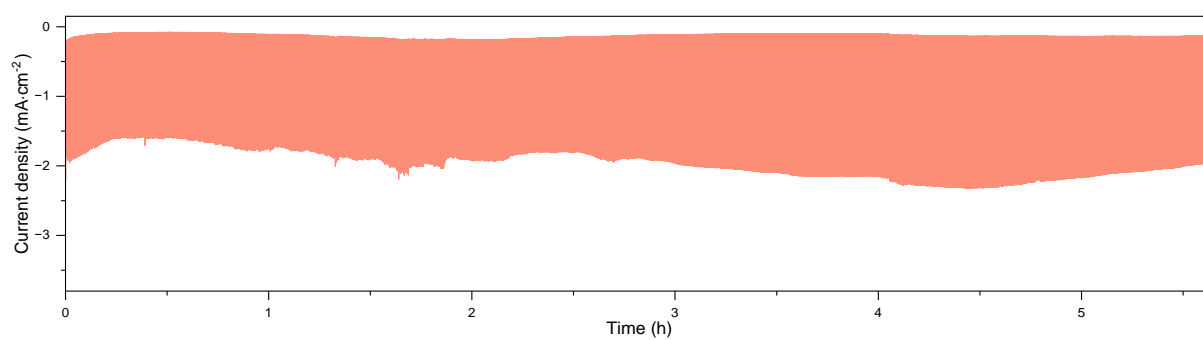
Figure S14. The photocurrent responses of $Fe_2O_3/Cu_2O/Cu$ photocathode under light irradiation at a potential of -0.95 V (vs. Fc/Fc^+) in CO_2-saturated 1.0 M tetrabutylammonium hexafluorophosphate in acetonitrile.
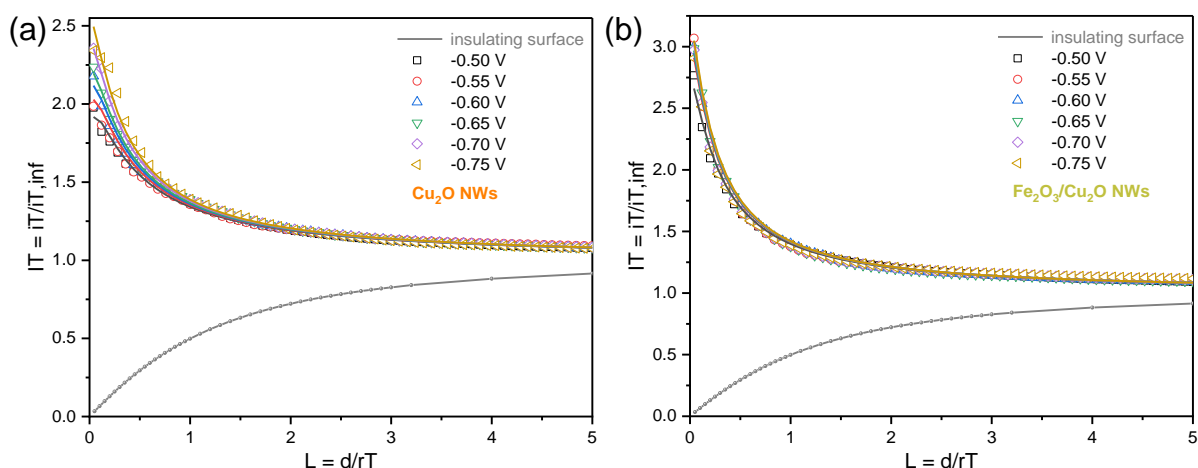
Figure S15. The normalized SECM approach curves in the feedback mode with Pt ultramicroelectrode approaching (a) Cu_2O nanowire and (b) Fe_2O_3/Cu_2O nanowire electrodes in 2 mM $Fe(C_5H_5)_2$ in acetonitrile solution.

The measurement procedure of the interface kinetic constant for Cu_2O/Cu and Fe_2O_3/Cu_2O photocathodes is as follows. First, the approach curves for two samples were recorded in 2 mM acetonitrile solution of ferrocene using the feedback mode of SECM. As shown in Figure S15, the normalized SECM approach curves for both Cu_2O/Cu nanowires and Fe_2O_3/Cu_2O nanowires exhibited the characteristics of interfacial charge transfer when the tip approached the sample surface. Apparently, the feedback current increased in dependence on the negative shift of the applied potential. Secondly, the interfacial apparent charge transfer rate constant κ, the interfacial effective charge transfer rate constant κ_{eff} and the apparent standard electron transfer rate constant k_e^0 at the photocathode/electrolyte interface could be calculated by fitting the above normalized SECM approach curves and according to equations (5) and (6):[14,15]

$$\kappa_{\text{eff}} = \frac{\kappa D_{\text{diffusion}}}{r_T} \qquad \text{S5}$$

$$\ln(\kappa_{\text{eff}}) = \ln k_e^0 - \alpha n f \eta \qquad \text{S6}$$

where $D_{diffusion}$ is the diffusion coefficient of the redox mediator，r_T is the radius of Pt UME, α is the charge transfer coefficient, n is the number of electron transfer at the interface reaction, f=nF/RT (F is faraday constant, R is gas constant, T is temperature), and η is the overpotential applied onto photocathode, respectively. Finally, the values of the apparent standard electron transfer rate constant k_e^0 at photoelectrode/electrolyte interface could be obtained from the linear relationship between $\ln(\kappa_{\text{eff}})$ and η.
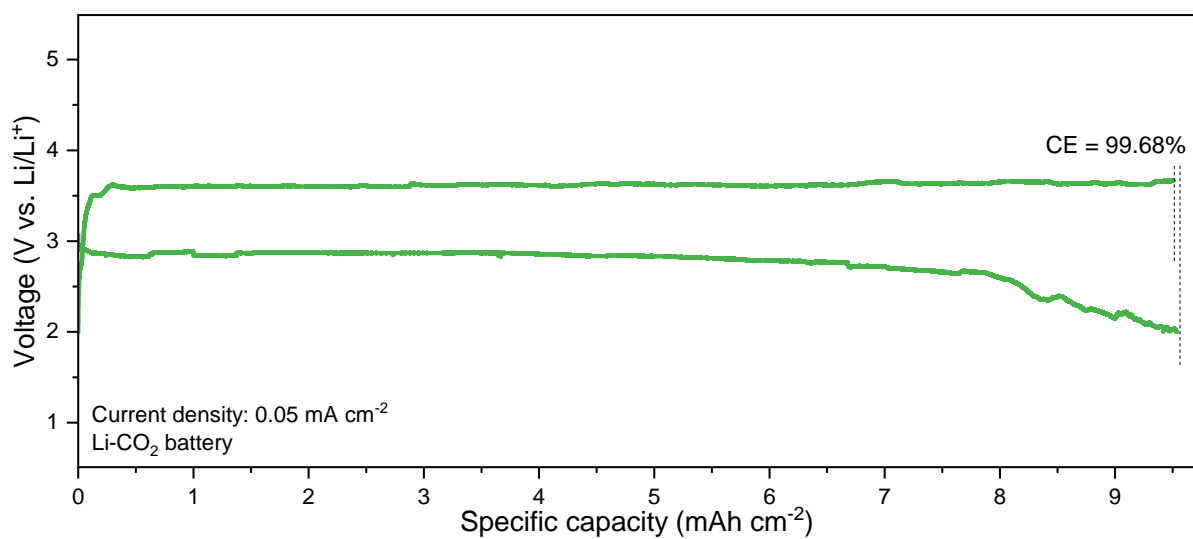
Figure S16. Deep discharge curves of the Li-CO$_2$ battery with a cut-off voltage of 2.0 V at 0.05 mA cm^{-2} under illumination.
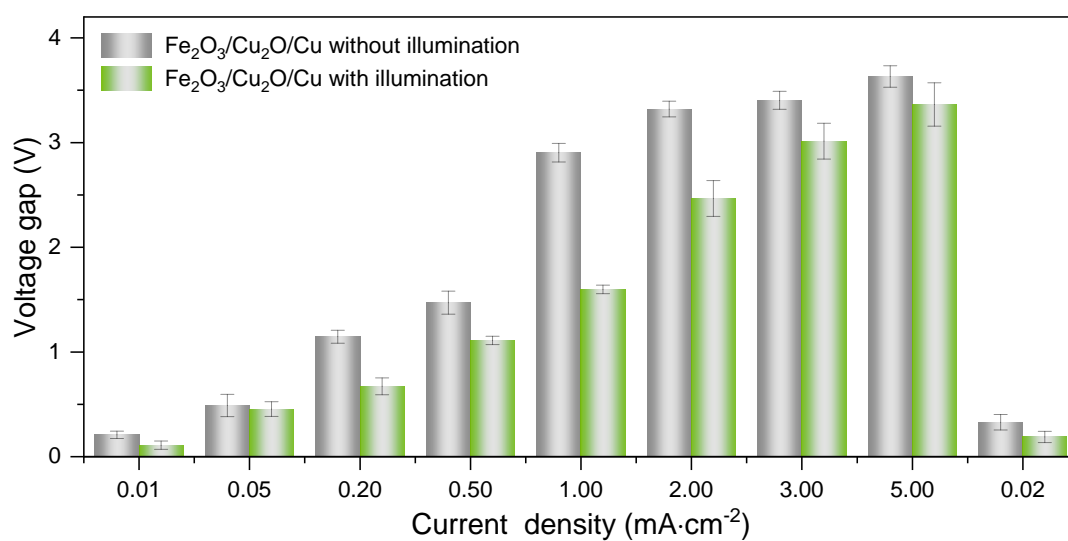
Figure S17. Voltage gap of the Li-CO$_2$ battery based on Fe$_2$O$_3$/Cu$_2$O/Cu cathode at different current densities with and without illumination.
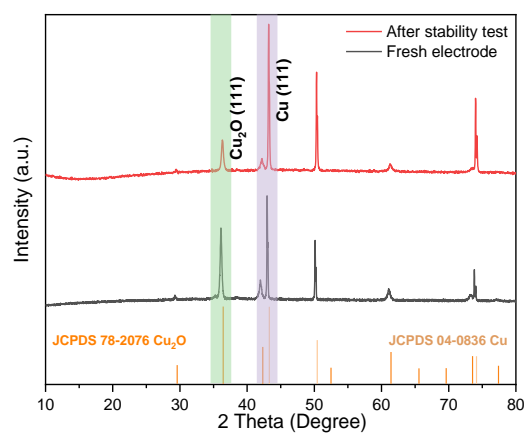
Figure S18. XRD patterns of Fe_2O_3/Cu_2O nanowires photocathode after long-term cycling.
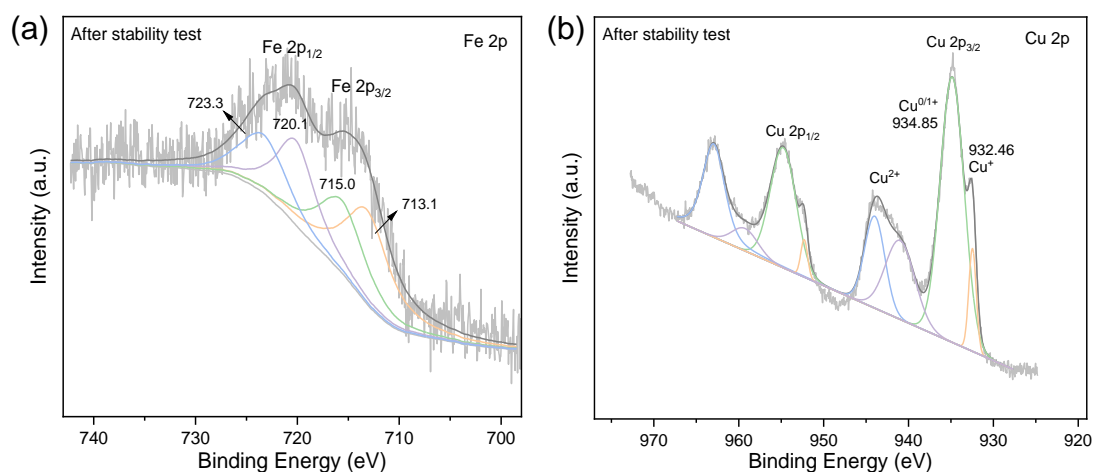
Figure S19. High-resolution XPS spectra of Fe_2O_3/Cu_2O nanowires photocathode after long-term cycling. (a) Fe 2p and (b) Cu 2p and the corresponding fitting results.

In addition, we performed phase stability characterization on Fe_2O_3/Cu_2O photocathode of Li-CO_2 battery after long-term cycling. The XRD result provided in Figure S18 shows that the intensity of the diffraction peak of Cu_2O was reduced compared to that of the fresh Fe_2O_3/Cu_2O sample (Figure S4c). Meanwhile, The Cu 2p XPS spectra further illustrate the decrease in the Cu^+ content and the increase in the Cu^0 and Cu^{2+} content in the after-cycling Fe_2O_3/Cu_2O samples (Figure S19), which may be attributed to the reduction/oxidation of Cu^+ by additional e^-/h^+ during discharge/charge process. Therefore, it leads to the degradation of the Fe_2O_3/Cu_2O heterojunction structure and then to the slow increase of the voltage gap during long-term cycling tests. This phenomenon has also been reported in the literatures about Cu_2O catalysts.[16,17]
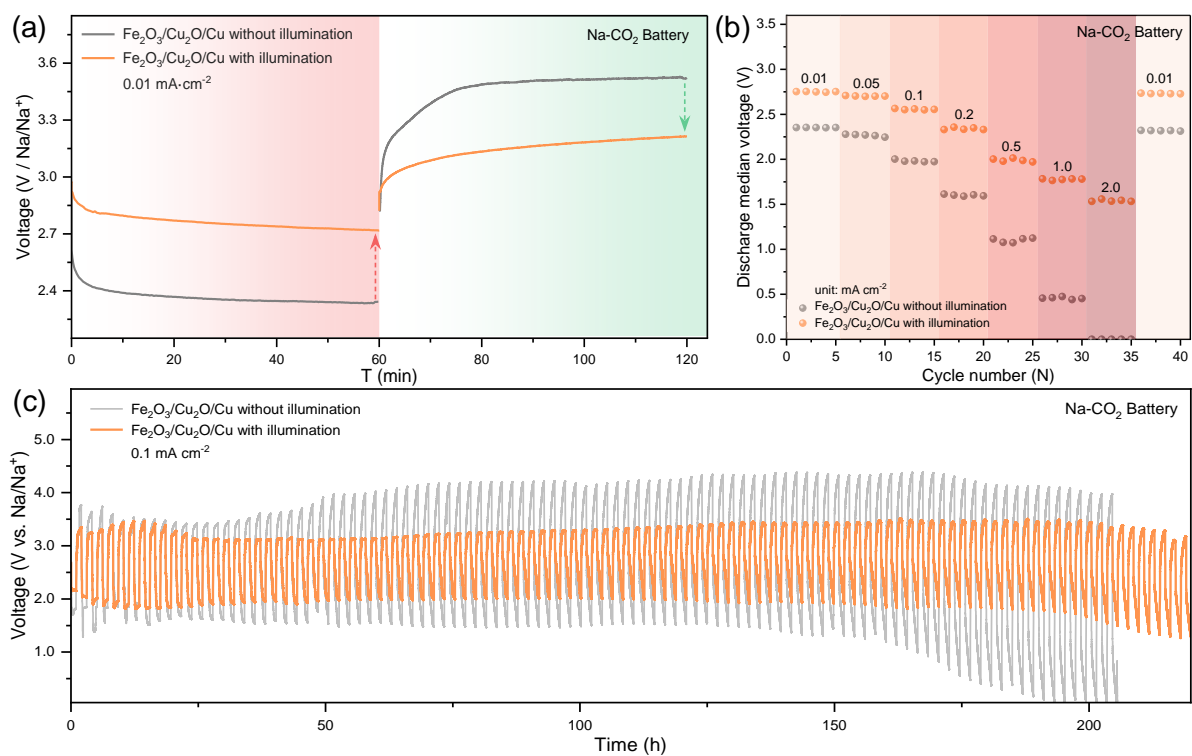
Figure S20. Electrochemical performance of the Na-CO$_2$ battery based on Fe$_2$O$_3$/Cu$_2$O nanowires type-II heterojunction photocathode with and without illumination. (a) Discharge/charge voltage curves at the current density of 0.01 mA cm^{-2}. (b) Rate performance. (c) Cycling curves in the current density of 0.10 mA cm^{-2}.
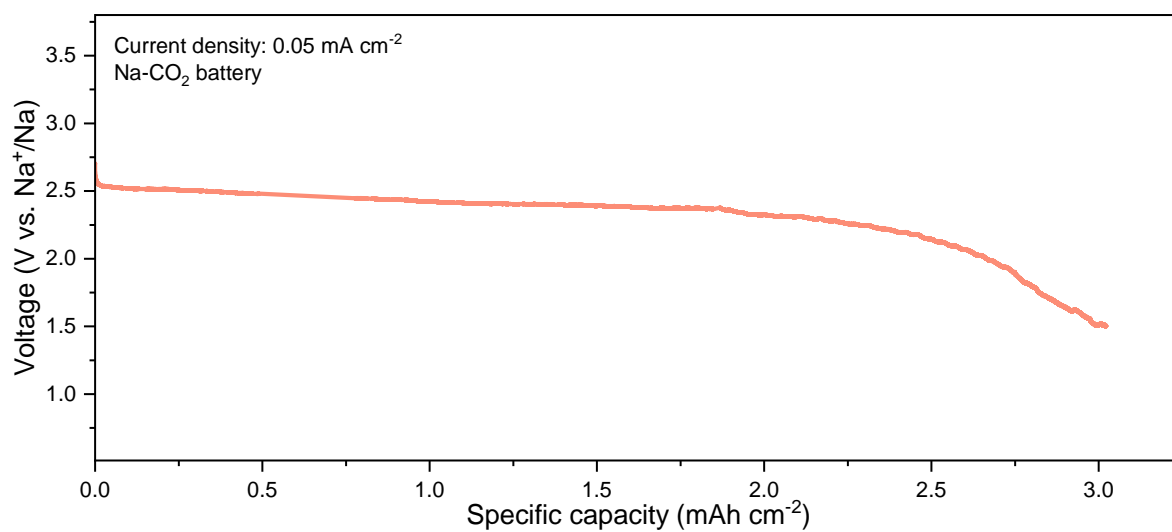
Current density: 0.05 mA cm^{-2}
Na-CO$_2$ battery

Figure S21. Deep discharge curves of the Na-CO$_2$ battery with a cut-off voltage of 1.5 V at 0.05 mA cm^{-2} under illumination.
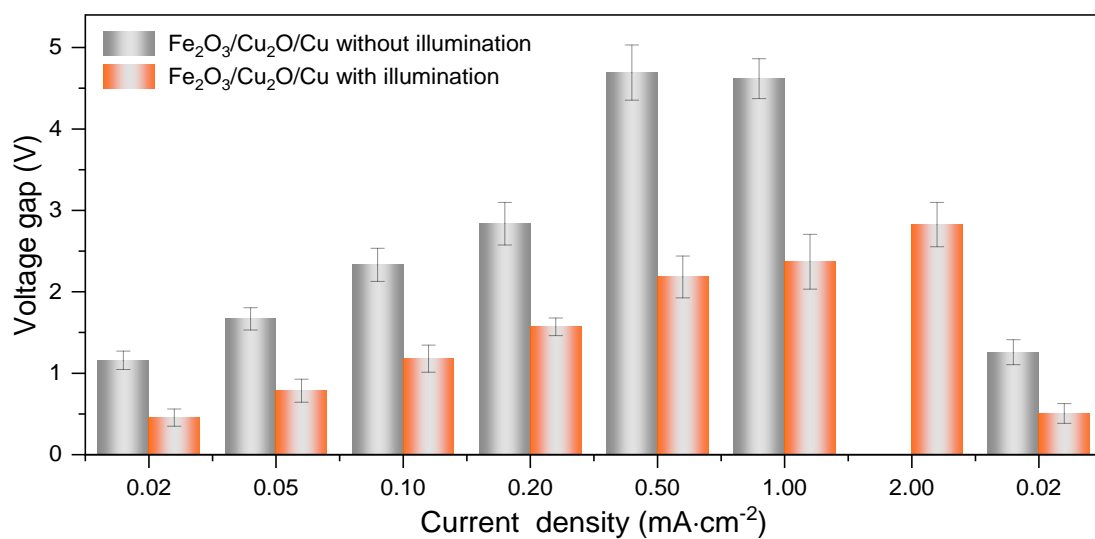
Figure S22. Voltage gap of at different current densities of the Na-CO$_2$ battery based on Fe$_2$O$_3$/Cu$_2$O/Cu cathode with and without illumination.

Figure S23. XRD patterns of Fe$_2$O$_3$/Cu$_2$O/Cu nanowires cathode at the different states (pristine, discharge and charge) under illumination.

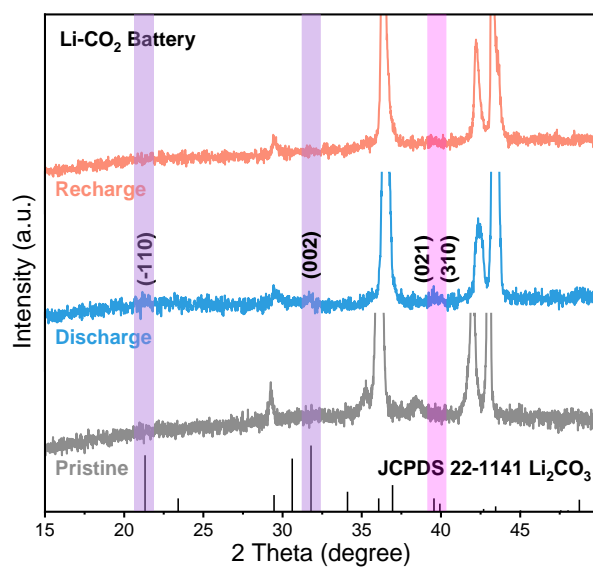**Figure S24.** Raman patterns of $Fe_2O_3/Cu_2O/Cu$ nanowires photocathode at the different states (pristine, discharge and charge) under illumination.
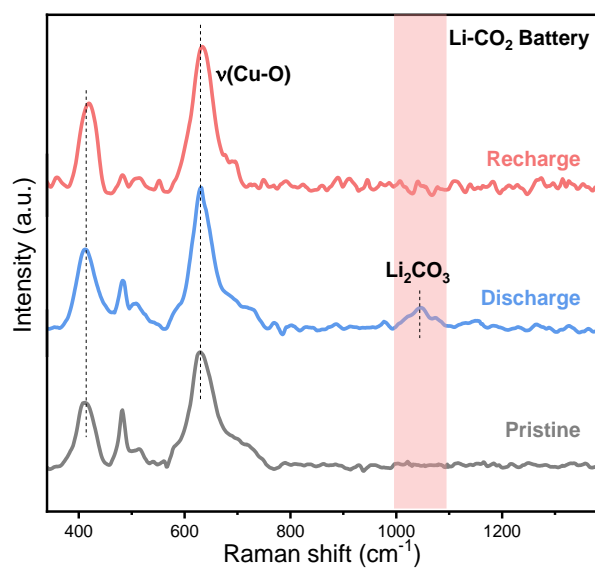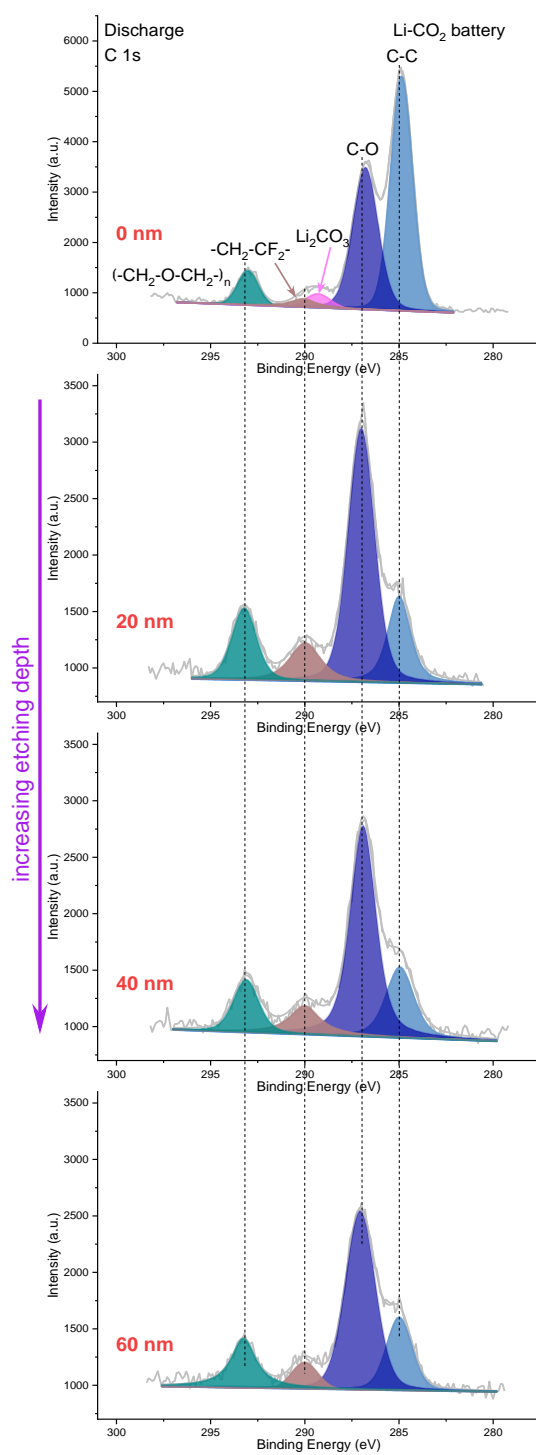
Figure S25. C 1s XPS depth profile analysis of $Fe_2O_3/Cu_2O/Cu$ nanowires photocathode in the discharge state after operating 10 h at 0.01 mA cm^2 current density.

The signal peaks of C-F, C-O bonding in C 1s XPS spectra in the discharge/charge state should be attributed to the adsorption of an abundant of electrolyte (1.0 M LiTFSI in TEGDME) on the Fe_2O_3/Cu_2O cathode. To further illustrate the effect of the electrolyte we selected the cathode in the discharge state and performed a depth profile analysis on it. Note that the

discharge operation time was extended appropriately compared to that of Figure 6c in order to more clearly observe the discharge products. As shown in Figure S25, we found that the surface of the Fe_2O_3/Cu_2O cathode in the discharge state exhibits a similar characterization with the C 1s XPS spectra in Figure 6c. The strong C-C and obvious Li_2CO_3 signal peak are all able to indicate the generation of the discharge product (Li_2CO_3+C). Subsequently, the Fe_2O_3/Cu_2O cathode was sequentially etched at the same position as above for 20 nm, 40 nm, and 60 nm depths and then performed the C 1s XPS characterization. It can be found that the C-C peak is obviously weakened and lower than the C-O peak after etching 20 nm, and the intensity of all signal peaks gradually decreases more obviously after etching 40 nm and 60 nm. Furthermore, the carbon peaks at 293.1 and 290.0 eV usually denote the presence of C-O, C-F species originating from TEGDME and LiTFSI, which are still present even after etching for 60 nm. We speculate that this may be due to the electrolyte attaching the surface of Fe_2O_3/Cu_2O and infiltrating the interior of the flocculated discharge products during the discharge process.
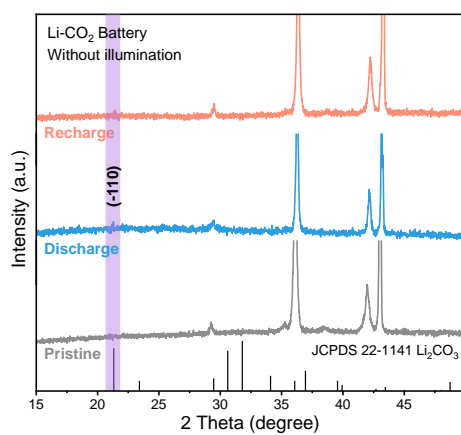
Figure S26. XRD patterns of $Fe_2O_3/Cu_2O/Cu$ nanowires cathode at the different states (pristine, discharge and charge) without illumination.
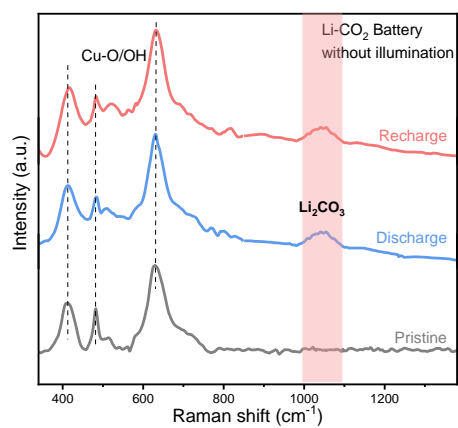
Figure S27. Raman patterns of Fe₂O₃/Cu₂O/Cu nanowires cathode at the different states (pristine, discharge and charge) without illumination.
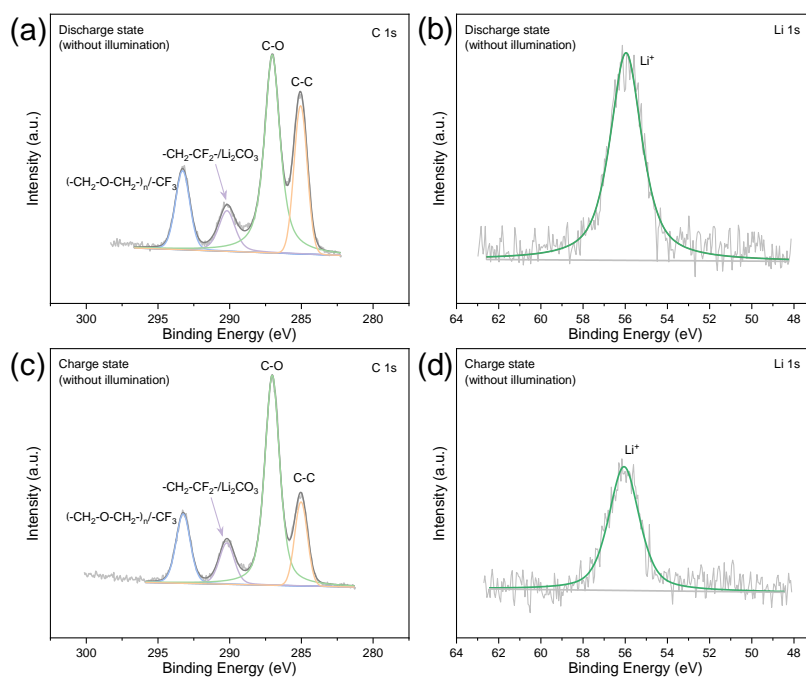
Figure S28. The high-resolution XPS spectra of $Fe_2O_3/Cu_2O/Cu$ nanowires cathode for $Li-CO_2$ battery without illumination. (a) C 1s and (b) Li 1s XPS at discharge state, (c) C 1s and (d) Li 1s XPS at charge state.
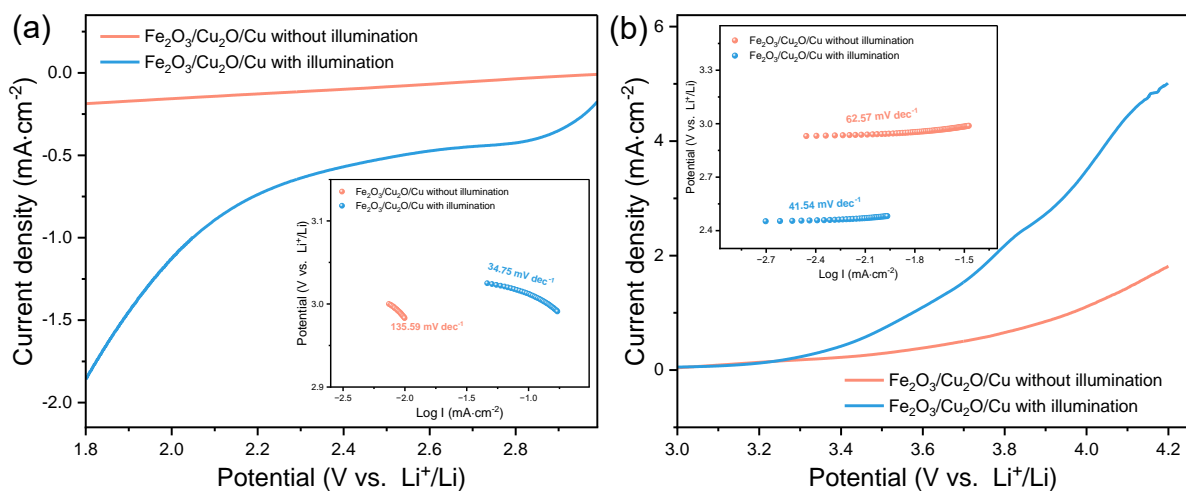
Figure S29. Linear sweep voltammetry (LSV) curves of CDRR (a) and CDER (b) employing Fe$_2$O$_3$/Cu$_2$O/Cu nanowires cathode with and without illumination at 10 mV s^{-1} in 1.0 M LiTFSI/TEGDME, the inset is corresponding Tafel curves.
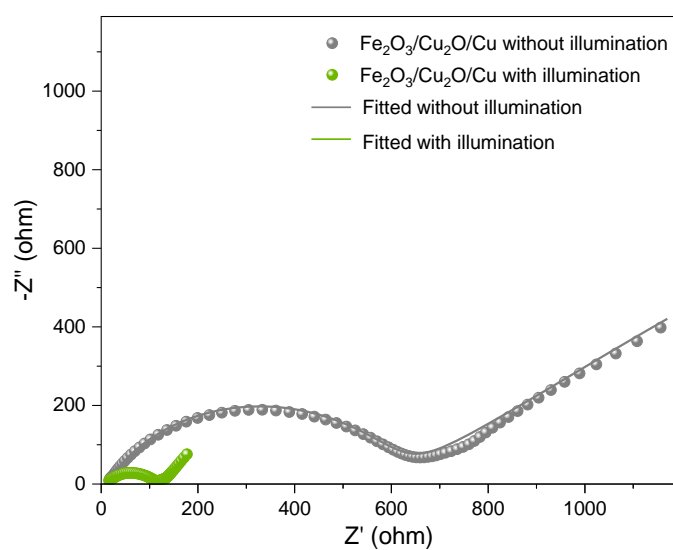
Figure S30. Electrochemical impedance spectra of Li-CO$_2$ battery with Fe$_2$O$_3$/Cu$_2$O/Cu nanowires cathode with and without illumination.
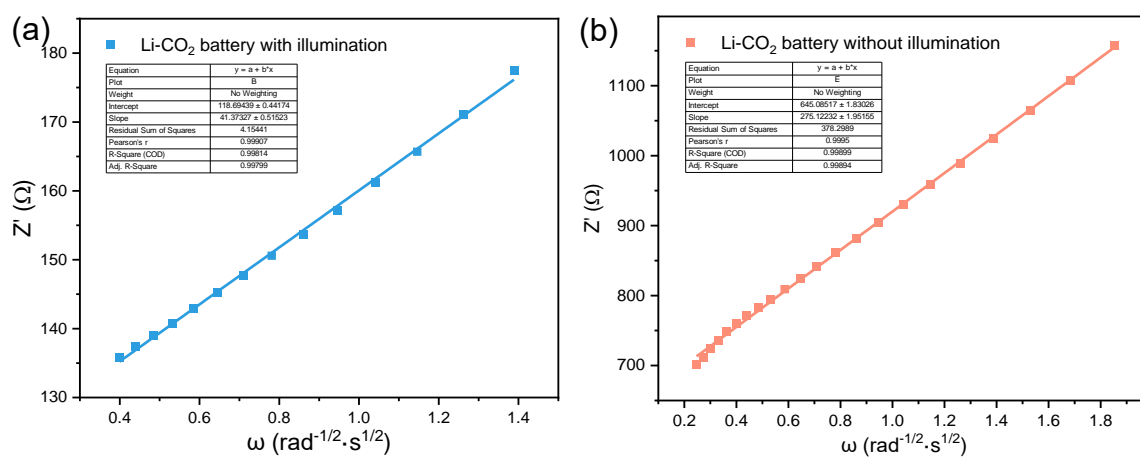
Figure S31. Warburg coefficient (σ) calculated from the EIS of Li-CO$_2$ battery based on Fe$_2$O$_3$/Cu$_2$O/Cu nanowires cathode (a) with and (b) without illumination.
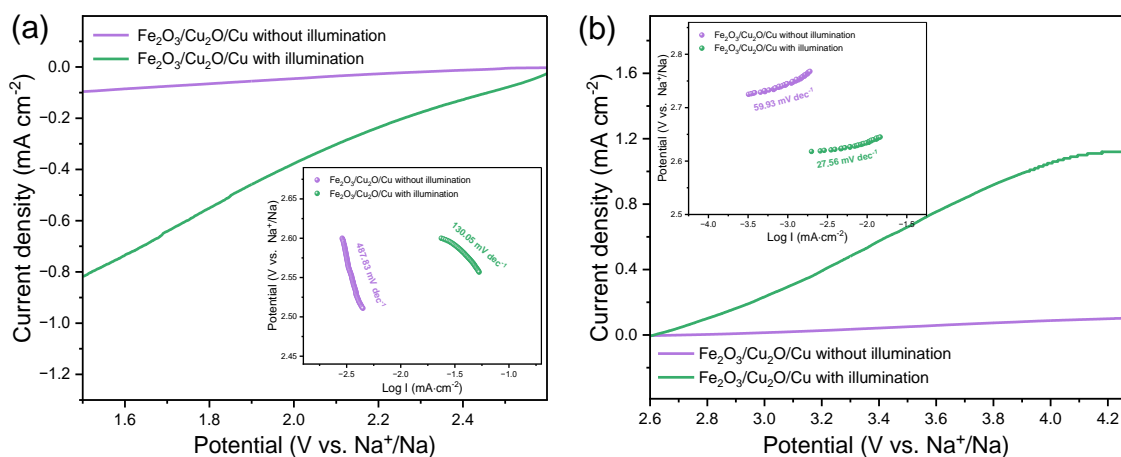
Figure S32. Linear sweep voltammetry (LSV) curves of CDRR (a) and CDER (b) employing Fe$_2$O$_3$/Cu$_2$O/Cu hybrid NWs with and without illumination at 10 mV s^{-1} in 1.0 M NaPF$_6$/EC+DMC (vol=1:1, with 5% FEC), the inset is corresponding Tafel curves.
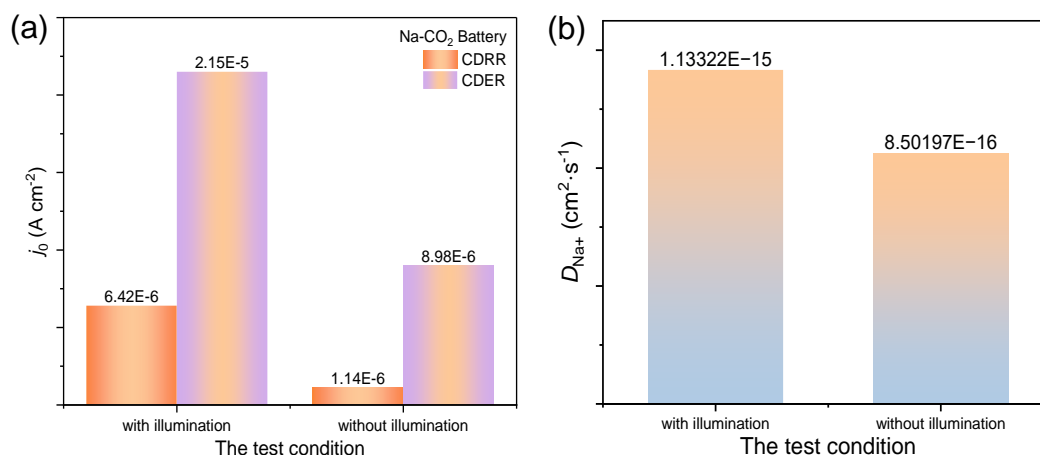
Figure S33. (e) Comparison of exchange current density (j_0) values of CDRR/CDER processes for Na-CO$_2$ battery with Fe$_2$O$_3$/Cu$_2$O/Cu cathode in different test condition. (f) Comparison of Na$^+$ diffusion coefficient of Na-CO$_2$ battery with Fe$_2$O$_3$/Cu$_2$O/Cu cathode in different test condition.

As shown in Figure S32, the current density of the Na-CO$_2$ battery in both the CO$_2$RR process and the CO$_2$ER process increases sharply due to the introduction of illumination, with an increase of 0.71 mA cm^{-2} and 0.97 mA cm^{-2} at the tested cut-off voltage compared to the dark state, respectively. Furthermore, the Tafel slop value in the CO$_2$RR and CO$_2$ER processes decreased from 487.83 to 130.05 mV dec^{-1} and from 59.93 to 27.56 mV dec^{-1} in the illumination, respectively. the corresponding exchange current densities also increased from 1.14×10^{-6} to 6.42×10^{-6} A cm^{-2} and from 8.95×10^{-6} to 2.15×10^{-5} A cm^{-2} (Fig. S33a). The diffusion coefficient of Na$^+$ (D_{Na^+}) was also increased due to the presence of illumination (Figure S33b, Figure S34). The smaller Tafel slope value, the higher exchange current density and the better Na$^+$ diffusion capacity confirmed the enhancement of reaction kinetics and electrode intrinsic activity in the CO$_2$RR and CO$_2$ER processes. It is noted that these above-mentioned values of exchange current density and ion diffusion coefficient are smaller than that of Li-CO$_2$ battery, indicating that the transport kinetics and diffusion rate of Na$^+$ are weaker than those of Li$^+$. This may be the intrinsic reason why the performance of light-assisted Na-CO$_2$ battery based on the same Fe$_2$O$_3$/Cu$_2$O photocathode is inferior that of light-assisted Li-CO$_2$ battery.

Figure S34. Electrochemical impedance spectra of Na-CO$_2$ battery with Fe$_2$O$_3$/Cu$_2$O/Cu NWs cathode with and without illumination.
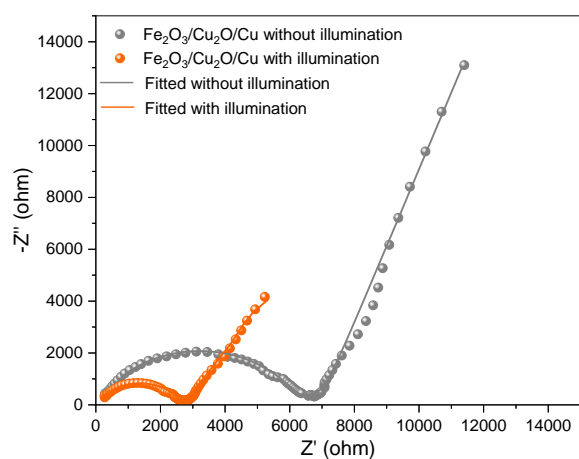
Figure S35. Optical photograph of Lithium foil corresponding to the dissected flexible quasi-solid-state Li-CO$_2$ pouch battery with the Fe$_2$O$_3$/Cu$_2$O/Cu nanowires cathode after cycle test at a current density of 0.05 mA·cm^{-2}.
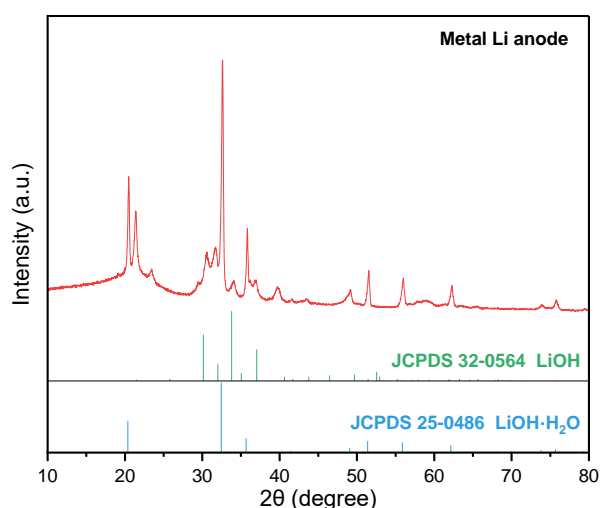
Figure S36. XRD pattern of the of the lithium anode (Figure S31) for the flexible quasi-solid-state Li-CO_2 pouch battery after stopping operation.

Meanwhile, in view of the excellent mechanical processability of the copper mesh support and the demand for flexible energy storage devices, the $Fe_2O_3/Cu_2O/Cu$ nanowire catalysts were extended to serve as a cathode for a flexible quasi-solid-state Li-CO_2 pouch battery with a length of 5.5 cm and a width of 4.3 cm. **Figure 7**a shows a schematic illustration of the flexible quasi-solid-state Li-CO_2 pouch battery. The cross-sectional SEM image of the solid electrolyte diaphragm in this structure shows that both sides of the polypropylene separator are uniformly coated with a 2 μm thick layer of LATP electrolyte to facilitate Li^+ transport during the discharge and charge process (Figure 7b). The pouch battery can normally power up a commercial light-emitting diodes (LED) lamp beads at various bending angles from 0° to 180° (Figure 7c-g). Even after taking damage (crimped, cut, recut and bent), the LED lamp beads powered by the pouch battery with Fe_2O_3/Cu_2O nanowires cathode still worked well (Figures 7h-j). Even when the pouch battery was crimped (Figure 7h), cut (Figure 7i), recut and bent (Figure 7j), the LED lamp beads could still work well. Meanwhile, the open-circuit voltage of the pouch battery also remained stable (Figure 7k). The Video S1 provided within the supporting information presents the whole process of the LED lamp beads being lit normally after the pouch battery was cut. Those results demonstrate the potential application prospects of the as-synthesized self-supporting electrode in the field of flexible electronic devices. The above-mentioned flexible Li-CO_2 pouch battery based on $Fe_2O_3/Cu_2O/Cu$ nanowires cathode exhibits superior cycling performance over 110 h in the presence of illumination at a current

42

density of 0.05 mA cm^{-2}. According to the discharge/charge curves provided in Figure 7l-n, the median discharge voltage of the flexible Li-CO$_2$ pouch battery only decreases by about 0.2 V during forty cycles, and the variation of the median charge voltage is basically negligible. The flexible Li-CO$_2$ pouch battery suddenly terminated after normally operating for 110 h. By dissecting the battery after stopping operation, we found that the main cause should be the severe corrosion of lithium metal by environmental moisture (Figures S35 and S36). To prove the durability of the Fe$_2$O$_3$/Cu$_2$O nanowire catalysts, the reassembly strategy was adopted here. The reassembled Li-CO$_2$ pouch battery based on the previous cathodes can continue to operate stably for approximately 70 h under the same test conditions (Figures 7m and 7n). Its discharge/charge curves are very similar to those of the initial state cathode.

Table S1. Literature comparison of the photoelectrochemical performances of CO_2 reduction producing CO in organic solvent or water solution.

References	Catalysts	Photocurrent /Potential	Product selectivity	Stability	Electrolyte
This work	**Fe$_2$O$_3$/Cu$_2$O/Cu**	**2.2 mA cm^{-2} /-1.2 V vs Fc/Fc$^+$**	**CO (93%)**	**5.2 h**	**1.0 M Bu$_4$NPF$_6$ in CH$_3$CN**
ACS Energy Lett. **2023**, 8, 1645−1651	CuIn$_{0.3}$Ga$_{0.7}$S$_2$	2 mA cm^{-2} /−2 V vs Fc/Fc$^+$	CO (87%)	1.1 h	0.1 M Bu$_4$NPF$_6$ in CH$_3$CN
ACS Catal. **2022**, 12, 12596−12606	C$_2$-Ru-MeCN^{2+}	50 µA cm^{-2} /−1.8 V vs Fc/Fc$^+$	CO (32%)	1 h	0.1 M Bu$_4$NPF$_6$ CH$_3$CN with 5% H$_2$O
J. Am. Chem. Soc. **2019**, 141, 10924−10929	Cu-MOF/Cu$_2$O	0.44 mA cm^{-2} /−2.27 V vs Fc/Fc$^+$	CO (17%)	400 s	0.1 M Bu$_4$NPF$_6$ in CH$_3$CN
J. Am. Chem. Soc. **2016**, 138, 1938−1946	Au/Cu$_2$O/Al:ZnO/TiO$_2$	1.79 mA cm^{-2} /−1.9 V vs Fc/Fc$^+$	CO (85-100%)	1.05 h	0.1 M Bu$_4$NPF$_6$ in CH$_3$CN
Angew. Chem. Int. Ed. **2016**, 55, 7388 −7392	TiO$_2$	0.45 mA cm^{-2} /−1.7 V vs Fc/Fc$^+$	CO (12%)	2 h	0.1 M Bu$_4$NPF$_6$ in CH$_3$CN/H$_2$O (19/1)
Energy Environ. Sci. **2015**, 8, 855	Au/Cu$_2$O/Al:ZnO/TiO$_2$ +Re(tBu-bipy)(CO)$_3$Cl	1.6 mA cm^{-2} /−1.73 V vs Fc/Fc$^+$	CO (100%)	5.5 h	0.1 M Bu$_4$NPF$_6$ and 7.5 M CH$_3$OH in CH$_3$CN
Small **2022**, 18, 2201882	Au/TiO$_2$/n$^+$p-Si	5.52 mA cm^{-2} /−0.8 V vs RHE	CO (86%)	20 h	0.1 M KHCO$_3$ solution
Small **2021**, 17, 2102957	CoPor-N$_3$ polymer	14 mA cm^{-2} /−0.5 V vs RHE	CO (96%)	20 min	0.5 M KHCO$_3$ solution
Joule **2020**, 4, 2149–2161	Si NW/Ni SA	1.1 mA cm^{-2} /−0.8 V vs RHE	CO (68%)	6 h	0.25 M KHCO$_3$ solution
Nano Lett. **2016**, 16, 5675−5680	Au$_3$Cu NP/Si NW	−0.20 V vs RHE	CO (80%)	18 h	0.1 M KHCO$_3$ solution

Table S2. Resistance and capacitance values obtained by fitting the complex plane impedance diagrams of Cu_2O and Fe_2O_3/Cu_2O electrodes.

sample	R_s (Ω cm^{-2})	$R_{ct,sc}$ (Ω cm^{-2})	$R_{ct,d}$ (Ω cm^{-2})	$C_{ct,sc}$ (μF cm^{-2})	$C_{ct,d}$ (μF cm^{-2})
Cu_2O	1.38	143.10	1878	430.53	70.98
Fe_2O_3/Cu_2O	1.45	38.92	1485	20.95	112.15

Note. $C_{ct,sc}$ and $C_{ct,d}$ is the real capacitance of the space charge of semiconductor and the real capacitance of the double layer at the semiconductor/electrolyte interface, respectively.

Table S3. Literature comparison of the discharge/charge performances of light-assisted Li-CO_2 battery with $Fe_2O_3/Cu_2O/Cu$ nanowires photocathode.

References	Catalysts	Self-supporting cathode (Y/N)	Overpotential of 1st cycle	Cycle performance (current density)	Performance of pouch battery
This work	$Fe_2O_3/Cu_2O/Cu$	Y	0.19 V/0.01 mA cm^{-2}	520 h (0.1 mA cm^{-2})	180 h (0.05 mA cm^{-2})
Small **2023**, 2300519	mixed-phase TiO_2	Y	0.75 V/0.025 mA cm^{-2}	580 h (0.025 mA cm^{-2})	-
Adv. Funct. Mater. **2022**, 32, 2210259	CoPc-Mn-O/rGO	N	0.05 V/0.01 mA cm^{-2}	60 h (0.1 mA cm^{-2})	-
Angew. Chem. Int. Ed. **2022**, 134, e202114612	CNT/C_3N_4	N	0.04 V/0.02 mA cm^{-2}	200 h (0.1 mA cm^{-2})	-
Angew. Chem. Int. Ed. **2022**, 61, e202201718	TNAs/AgNPs	N	0.37 V/0.01 mA cm^{-2}	200 h (0.1 mA cm^{-2})	-
Small **2021**, 17, 2100642	TiO_2/CC	Y	0.08 V/0.01 mA cm^{-2}	60 h (0.1 mA cm^{-2})	60 h (0.01 mA cm^{-2})
Angew. Chem. Int. Ed. **2020**, 59, 19518-19524	In_2S_3/CNT/SS	Y	0.06 V/0.01 mA cm^{-2}	50 h (0.1 mA cm^{-2})	20 h
J. Mater. Chem. A **2020**, 8, 14799-14806	SiC/RGO	N	0.42 V/0.012 mA cm^{-2}	160 h (0.012 mA cm^{-2})	-

Table S4. The value of R_s and R_{ct} Li-CO$_2$ battery with Fe$_2$O$_3$/Cu$_2$O/Cu nanowires cathode with and without illumination.

	R_s (Ω)	R_{ct} (Ω)
With illumination	24	126
Without illumination	32	680

Reference

[1] L. Xiang, J. Guo, C. Wu, M. Cai, X. Zhou N. Zhang, *J. Mater. Res.* 2018, **33**, 2264–2280.

[2] X. Deng, R. Li, S. Wu, L. Wang, J. Hu, J. Ma, W. Jiang, N. Zhang, X. Zheng, C. Gao, L. Wang, Q. Zhang, J. Zhu, Y. Xiong, *Journal of the American Chemical Society* **2019** 141, 10924.

[3] J. Gao, J. Li, Y. Liu, M. Xia, Y. Finfrock, S. Zakeeruddin, D. Ren, M. Grätzel, *Nature Communications* **2022** 13, 5898.

[4] G. Kresse, J. Furthmüller, *Computational Materials Science* 1996, 6, 15.

[5] G. Kresse, J. Furthmüller, *Physical Review B* 1996, 54, 11169.

[6] J. Perdew, K. Burke, M. Ernzerhof, *Physical Review Letters* 1997, 78, 1396.

[7] G. Kresse, D. Joubert, *Physical Review B* 1999, 59, 1758.

[8] P. Blöchl, *Physical Review* B 1994, 50, 17953.

[9] Yasuo Matsubara, *ACS Energy Letters* **2017**, 2, 1886.

[10] N. Mendieta-Reyes, W. Cheuquepán, A Rodes, R. Gómez, *ACS Catalysis* **2020**, 10, 103.

[11] Y. Liu, M. Xia, D. Ren, S. Nussbaum, J. Yum, M. Grätzel, N. Guijarro, K. Sivula, *ACS Energy Letters* **2023**, 8, 1645.

[12] J. Luo, X. Xia, Y. Luo, C. Guan, J. Liu, X. Qi, C. Ng, T. Yu, H. Zhang, H. Fan, *Advanced Energy Materials* **2013** 3, 737.

[13] Q. Zhu, K. Zhu, M. Cai, Y. Zhang, Z. Shao, M. Jiang, X. Wang, Z. Geng, X. Wu, M. Li, *Nano Research* **2022**, 15, 7099.

[14] J. Lu, B. Zhang, H. Yuan, X. Xu, K. Cao, J. Cui, S. Liu, Y. Shen, Y. Cheng, J. Xu, *Journal of Physical Chemistry C* **2014** 118, 14739.

[15] Z. Yu, Q. Huang, X. Jiang, X. Lv, X. Xiao, M. Wang, Y. Shen, G. Wittstock, *Analytical Chemistry* **2021** 93, 12221.

[16] S. Ding, X. Bai, L. Cui, Q. Shen, X. Zhang, H. Jia, J. Xue, ACS Appl. Nano Mater. 2023, 6, 12, 10539–10550.

[17] Z. Zheng, B. Huang, Z. Wang, M. Guo, X. Qin, X. Zhang, P. Wang, Y. Dai, J. Phys. Chem. C 2009, 113, 32, 14448–14453.